Chemical Science

ROYAL SOCIETY OF CHEMISTRY

EDGE ARTICLE

View Article Online
View Journal | View Issue

Open Access Article. Published on 14 May 2024. Downloaded on 1/12/2026 4:43:35 AM.
This article is licensed under a Creative Commons Attribution-NonCommercial 3.0 Unported Licence.

Check for updates

Cite this: *Chem. Sci.*, 2024, **15**, 9240

All publication charges for this article have been paid for by the Royal Society of Chemistry

Bidirectional photomagnetism, exciplex fluorescence and dielectric anomalies in a spin crossover Hofmann-type coordination polymer†

Yan-Ru Chen, Ting-Ting Ying, Yan-Cong Chen, Pei-Yu Liao, Zhao-Ping Ni * and Ming-Liang Tong *

Stepped spin crossover (SCO) complexes with three or more spin states have promising applications in high-order data storage, multi-switches and multi-sensors. Further synergy with other functionalities, such as luminescence and dielectric properties, will provide a good chance to develop novel multifunctional SCO materials. Here, a bent pillar ligand and luminescent pyrene guest are integrated into a three-dimensional (3D) Hofmann-type metal–organic framework (MOF) $[Fe(dpoda)\{Au(CN)_2\}_2]\cdot$pyrene (dpoda = 2,5-di-(pyridyl)-1,3,4-oxadiazole). The magnetic data show an incomplete and two-step SCO behavior with the sequence of 1 ↔ 1/2 ↔ 1/4. The rare bi-directional light-induced excited spin-state trapping (LIESST) effect and light-induced stepped thermal relaxation after LIESST are observed. The pyrene guests interact with dpoda ligands *via* offset face-to-face π···π interactions to form intermolecular exciplex emissions. The competition between thermal quenching and stepped SCO properties results in a complicated and stepped exciplex fluorescence. Moreover, the stepped dielectric property with higher dielectric permittivity at lower temperature may be related to the more frustrated octahedral distortion parameters in the intermediate spin states. Hence, a 3D Hofmann-type MOF with bent pillar ligands and fluorescent guests illustrates an effective way for the development of multifunctional switching materials.

Received 15th January 2024
Accepted 9th May 2024

DOI: 10.1039/d4sc00331d

rsc.li/chemical-science

Introduction

Spin crossover (SCO) complexes are typical multi-responsive molecular switches that exhibit magnetic, structural and spectroscopic changes triggered by external stimuli such as temperature, light irradiation, pressure or guest molecules, and have potential applications in data storage, displays, switches and sensors.[1–9] Most SCO materials only show an entropy-driven spin transition between high-spin (HS) and low-spin (LS) states. However, additional intermediate spin states can be observed as collective phenomena in two-step or multi-step SCO compounds, which result from symmetry breaking to generate unique SCO sites in different spin states.[10,11] Such stepped SCO complexes provide a good platform for the study of multifunctional materials with new potential applications in high-order data storage, multi-switches and multi-sensors.[12–16]

Since the discovery of the light-induced excited spin-state trapping (LIESST) effect in 1984, light irradiation has become an effective tool to regulate spin states.[17] The transitions from the LS to the light-induced HS* state (LIESST) and from the HS* to the LS state (reverse-LIESST) can be achieved by irradiation with different wavelengths of light.[18–20] However, the LIESST and reverse-LIESST effects can only switch between two electric states. Stepped SCO compounds may provide a chance to observe the unique bi-directional LIESST effect, which can directly regulate the tristability between the ground intermediate spin state and the light-induced HS* and LS* states.[21–24] Moreover, the rare phenomenon of stepped thermal relaxation after LIESST has been observed in some stepped SCO compounds.[25–28] Hence, the stepped SCO complexes provide a possibility for the development of new generation photo-responsive magnetic materials with multi-addressing capabilities, which have promising applications in quantum logic gates and spintronic devices.[29]

It is well known that accompanying the spin state change are often dramatic physical responses in the structural, optical and electrical properties, which provide a chance to produce a luminescence response in a synergetic way. Hence, luminescent SCO materials have been actively pursued in the past decade.[30,31] Luminophores can be incorporated into the SCO materials by physical or chemical methods. The latter can

Key Laboratory of Bioinorganic and Synthetic Chemistry of Ministry of Education, School of Chemistry, IGCME, Guangdong Basic Research Center of Excellence for Functional Molecular Engineering, Sun Yat-Sen University, Guangzhou 510275, P. R. China. E-mail: nizhp@mail.sysu.edu.cn; tongml@mail.sysu.edu.cn

† Electronic supplementary information (ESI) available: Additional structural and fluorescence figures and crystallographic tables. CCDC 2322894–2322896, 2340544, 2345335, 2345336 and 2352145–2352148. For ESI and crystallographic data in CIF or other electronic format see DOI: https://doi.org/10.1039/d4sc00331d

© 2024 The Author(s). Published by the Royal Society of Chemistry

Open Access Article. Published on 14 May 2024. Downloaded on 1/12/2026 4:43:35 AM.
This article is licensed under a Creative Commons Attribution-NonCommercial 3.0 Unported Licence.

combine the luminescent unit with the SCO centres into a single entity in a covalent bond, counterion or guest manner.[32–43] For example, exciplex fluorescence is red-shifted and often with a long lifetime in comparison with monomer fluorescence, which has received great attention in the fields of exciplex-based organic light-emitting materials and devices.[44–47] The pyrene molecule as a typical intermolecular exciplex was introduced into a three-dimensional (3D) Hofmann-type metal–organic framework (MOF) [Fe(bpben){Au(CN)$_2$}$_2$] (bpben = 1,4-bis(4-pyridyl)benzene), which exhibited synergy between exciplex fluorescence and SCO properties.[48]

Herein, the pyrene guest is introduced into a 3D Hofmann-type MOF with a bent pillar ligand to form a solvent-free clathrate [Fe(dpoda){Au(CN)$_2$}$_2$]·pyrene (**1**, dpoda = 2,5-di-(pyridyl)-1,3,4- oxadiazole), which exhibits an incomplete and two-step SCO behavior. The rare bi-directional LIESST and stepped thermal relaxation after LIESST are observed. The variable-temperature luminescence properties of **1** and its diamagnetic isostructural derivative [Zn(dpoda){Au(CN)$_2$}$_2$]·pyrene (**2**) suggest that the stepped exciplex fluorescence is correlated with two-step SCO behavior. Moreover, the dielectric anomaly seems to be related to the more frustrated octahedral distortion parameters in the intermediate spin states, which provide an effective strategy for the development of multifunctional optomagnetic and electromagnetic materials.

Results and discussion

Yellow/white crystals of **1**/**2** were synthesized by slow diffusion of Fe(ClO$_4$)$_2$·6H$_2$O/Zn(ClO$_4$)$_2$·6H$_2$O, K[Au(CN)$_2$] and the dpoda ligand in a 1 : 2:1 molar ratio along with an excess of pyrene in *N*,*N*-diethylformamide/ethanol solution. Thermogravimetric (TG) analysis illustrates that **1**/**2** can be thermally stable up to 226/232 °C (Fig. S5 and S6†), which precludes the presence of solvent molecules. The pyrene molecules begin to escape from the lattice upon heating and then the frameworks of **1** and **2** collapsed at 414 and 454 °C, respectively.

Crystal structure

Single-crystal X-ray diffraction (SC-XRD) was performed at 260, 203, 198, 145 and 100 K to reveal symmetric breaking in **1**. The crystal data of **2** at the corresponding temperatures illustrate that **2** and **1** are isostructural except for metal ions. At 260 K, **1** and **2** crystallize in the orthorhombic space group *Pbca* (Table S1 and S2†). The asymmetric unit of **1**/**2** is composed of two crystallographically unique Fe(II)/Zn(II) ions, two dpoda ligands, four [Au(CN)$_2$]$^-$ linkers and two pyrene guests (Fig. S7 and S8†), in which one pyrene is disordered over two positions with a ratio of 61 : 39 for **1** and 50 : 50 for **2**. Each Fe(II)/Zn(II) ion in **1**/**2** is coordinated equatorially by four [Au(CN)$_2$]$^-$ linkers, resulting in an undulated Hofmann layer along the *ab* plane (Fig. 1). The organic bridging ligands thread through one Hofmann layer and connect two adjacent layers along the *c* axis to form a two-fold interpenetrating 3D Hofmann-type MOF with pcu topology (Fig. S11†). Strong aurophilic interactions (3.03 and 3.09 Å in **1** and 3.03 and 3.10 Å in **2**) between two 3D frameworks are observed (Fig. 1 and Table S3, S4†).

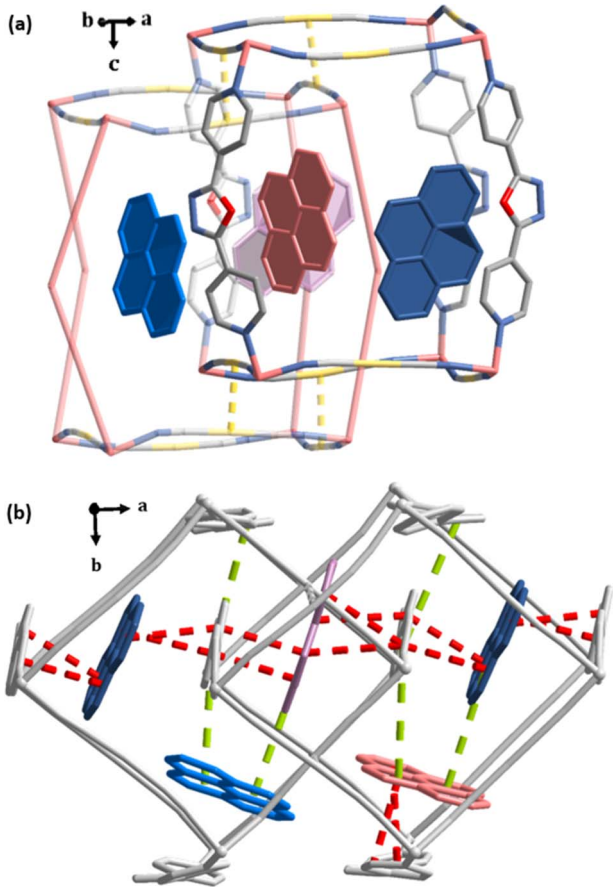

Fig. 1 (a) Crystal structure of **1** at 100 K. Hydrogen atoms are omitted for clarity. The dpoda ligands in one interpenetrated framework are simplified as the pink lines. Four crystallographically unique pyrene guests are distinguished by four different colors. Color codes: Fe, pink; Au, yellow; C, gray; N, blue; O, red. (b) Structural illustration of offset face-to-face π···π interactions (red dashed lines) and C–H···π interactions (green dashed lines) in **1** along the *c* axis. The interpenetrated frameworks are shown in gray.

Upon cooling, the diamagnetic derivative **2** remains in the same space group at 203, 198, 145 and 100 K. In contrast, symmetric breaking is observed in **1**, in which the space group changes from the centrosymmetric *Pbca* at 203 K to the chiral $P2_12_12_1$ at 198 K, 145 and 100 K. Accordingly, the number of crystallographically unique Fe(II) ions changes from 2 to 4 (Table S1†). Since disordered pyrene becomes ordered at lower temperatures in **1**, four unique dpoda ligands and pyrene guests with different orientations result in the absence of an inversion center and glide plane, leading to a chiral space group at 198, 145 and 100 K. In contrast, such results have not been observed in **2** (Table S2†), in which one pyrene is still disordered over two positions with a ratio 50 : 50 at low temperatures. Compared to 260 K, the unit cell volume of **1** is decreased by 1.6%, 2.1%, 4.1% and 5.9% at 203, 198, 145 and 100 K, respectively, indicating an obvious volume change. In contrast, the unit cell volume of **2** slightly decreases upon cooling and the total volume change

Open Access Article. Published on 14 May 2024. Downloaded on 1/12/2026 4:43:35 AM. This article is licensed under a Creative Commons Attribution-NonCommercial 3.0 Unported Licence.

from 260 K to 100 K is only 0.8%, which is mainly due to thermal contraction.

The structural parameters were further compared to structurally reveal the presence of SCO behavior. The detailed bond distances and angles are listed in Table S3 and S4.† At 260 K, the average <Fe–N> bond distances are 2.165 and 2.170 Å for Fe1 and Fe2, respectively, indicating that the Fe(II) ions are in the HS state. At 203 K, the average <Fe1–N> bond distance decreases to 2.100 Å corresponding to the mixed spin state, while the Fe2 ion is still in the HS state with <Fe2–N> = 2.166 Å. Upon cooling to 198 K, four crystallographically unique Fe(II) ions appear. The average Fe–N bond distances are 2.015, 2.155, 2.160 and 2.151 Å for Fe1–Fe4, respectively, which is close to that of the $HS_{0.75}LS_{0.25}$ state. These <Fe–N> values further change to 1.960, 2.013, 2.160 and 2.136 Å at 145 K, illustrating an $HS_{0.5}LS_{0.5}$ state. At 100 K, the average <Fe–N> bond distances of Fe1–Fe4 sites are 1.960, 1.988, 2.160 and 1.983 Å, respectively, corresponding to three LS ions and one HS Fe(II) ion. Hence, Fe1, Fe2 and Fe4 ions exhibit different SCO trends, while the Fe3 ion remains in the HS state.

The presence of a pyrene guest leads to abundant π···π interactions in **1** and **2**. At 260 K, the asymmetric units of **1** and **2** are composed of two crystallographically unique dpoda ligands, which are almost perpendicular to each other (Fig. S7 and S8†). Accordingly, two pyrene guests are also almost perpendicular to each other, in which the disordered pyrene is nearly parallel to the dpoda ligand along the *bc* plane (Fig. S12 and S13†). Four benzene units of disordered pyrene in **1** and **2** are effectively involved in the formation of four sets of offset face-to-face π···π interactions along the *a* axis with two adjacent 1,3,4-oxadiazole and pyridine units in two dpoda ligands from two 3D frameworks (Fig. S12, S13 and Table S5, S7†). Under the influence of host–guest interactions, the dpoda ligand along the *bc* plane has small dihedral angles between 1,3,4-oxadiazole and each pyridine (2.88/5.61° in **1** and 6.41/2.50° in **2** at 260 K). One pyridine unit in this dpoda ligand forms a C–H···π interaction with the 1,3,4-oxadiazole unit from the other framework, illustrating the host–host interaction in **1** and **2** (Fig. S12, S13 and Table S6, S8†). Since the dpoda ligand is bent, a relatively large void is left for the ordered pyrene. The ordered pyrene in **1** at 260 K becomes involved in C–H···π interactions with the disordered pyrene and pyridine unit of the dopda ligand, illustrating the weak guest–guest and host–guest interactions, respectively (Fig. S12 and Table S6†). However, one additional offset face-to-face π···π interaction is observed between the ordered pyrene and 1,3,4-oxadiazole unit of the dpoda ligand in **2** at 260 K (Fig. S13 and Table S7†). The intermolecular interactions in **1**/**2** at 203 K are similar to those at 260 K, in which their structural parameters are slightly changed upon cooling (Fig. S14 and S15†).

Accompanying the volume contraction and symmetry breaking, more π···π interactions appear in **1** at lower temperatures. The asymmetric unit of **1** in the chiral $P2_12_12_1$ space group contains four unique pyrene guests and four dpoda ligands. The disordered pyrene at 260 and 203 K becomes two ordered molecules at 198, 145 and 100 K, which become involved in effective offset face-to-face π···π interactions between the host and guest along the *a* axis (Fig. S16, S18 and S20†). Meanwhile, the relatively free pyrene at 260 and 203 K becomes two unique guests at lower temperature. The C–H···π interactions observed at 260 and 203 K are still present at 198, 145 and 100 K (Fig. S16, S18 and S20†). Moreover, one pyrene forms an additional offset face-to-face π···π interaction with the 1,3,4-oxadiazole unit of the dpoda ligand at 198 and 145 K (Fig. S16 and S18†). At 100 K, it becomes involved in an additional offset face-to-face π···π interaction with the pyridine unit of the dpoda ligand (Fig. S20 and Table S21†). Since the unit cell volume of **2** is only slightly decreased, the numbers of offset face-to-face π···π interactions and C–H···π interactions remain the same at five temperatures (Fig. S13, S15, S17, S19 and S21†). In contrast, an increase in offset face-to-face π···π interactions for one ordered pyrene is observed in **1** (Fig. S16, S18 and S20†), which is associated with the obvious volume change. Hence, four unique dpoda ligands with different orientations within and between the ligands and four pyrene guests with different orientations lead to abundant host-guest, guest–guest and host–guest interactions with different structural parameters in **1** at lower temperatures.

Photomagnetic properties

Variable-temperature magnetic susceptibility data at 2 K min^{-1} revealed an incomplete and two-step SCO behavior in the temperature range of 10–300 K (Fig. 2 and S22†). The $\chi_M T$ value is 3.76 cm^3 K mol^{-1} at 300 K, indicating that all the Fe(II) ions are in the HS state. It remains in the HS state till 255 K and then gradually decreases to 1.82 cm^3 K mol^{-1} at 125 K. Upon further cooling, it abruptly drops to 1.12 cm^3 K mol^{-1} at 105 K and then gradually decreases to 0.73 cm^3 K mol^{-1} at 10 K, illustrating an incomplete SCO behavior. The subsequent SCO curve in the warming mode is consistent with that in the cooling mode, which excludes the presence of thermal hysteresis. The differential magnetic curve exhibits two peaks at 117 and 204 K, indicating a two-step SCO behavior. The spin

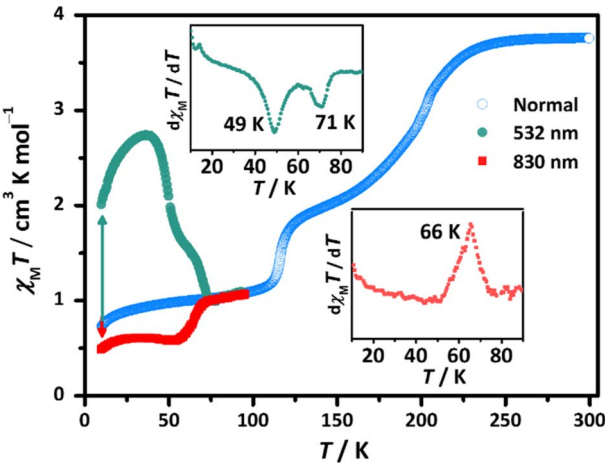

Fig. 2 Variable-temperature magnetic susceptibility data (blue) and bidirectional photomagnetic data of **1** irradiated at 532 (green) and 830 nm (red) at 2 K min^{-1}. Inset: the first derivative curves of photomagnetic data.

 © 2024 The Author(s). Published by the Royal Society of Chemistry

Open Access Article. Published on 14 May 2024. Downloaded on 1/12/2026 4:43:35 AM.
This article is licensed under a Creative Commons Attribution-NonCommercial 3.0 Unported Licence.

sequence is $\gamma_{HS} = 1 \leftrightarrow 1/2 \leftrightarrow 1/4$. However, the crystal data at 198 K clearly exhibit four unique Fe ions with the average Fe–N bond distances of 2.015, 2.155, 2.160 and 2.151 Å, suggesting the presence of the $HS_{0.75}LS_{0.25}$ state. Unfortunately, the magnetic curve does not show any obvious plateau near 198 K. Hence, three-step SCO behavior with the sequence of $\gamma_{HS} = 1 \leftrightarrow 3/4 \leftrightarrow 1/2 \leftrightarrow 1/4$ is hidden, which is revealed only by the combination of the magnetic and crystal data.

The photomagnetic experiments were performed on a small amount of microcrystalline sample at 10 K to explore a unique bidirectional LIESST effect (Fig. 2).[21–24] By irradiation with a 532 nm laser at 10 K, the $\chi_M T$ value gradually increases and finally reaches a photostationary state of 2.01 cm^3 K mol^{-1} after 2 h, indicating the LIESST effect. Then, the green light was turned off for the following magnetic susceptibility measurement in the warming mode. The $\chi_M T$ value increases to 2.74 cm^3 K mol^{-1} at 36 K, which originated from the zero-field splitting effect of HS Fe(II) ions. Subsequently, the $\chi_M T$ value rapidly decreases with an obvious slope change and goes back to the original thermal SCO curve at 74 K. Two minima of $\partial(\chi_M T)/\partial T$ at 49 and 71 K clearly illustrate the two-step spin transition process with an intermediate 1HS : 1LS state. Hence, the unique stepped thermal relaxation after LIESST is observed, which is rare in the SCO field.[25–28]

The reverse-LIESST effect is further explored by irradiating with an 830 nm laser at 10 K. The $\chi_M T$ value gradually decreases from 0.73 cm^3 K mol^{-1} to 0.48 cm^3 K mol^{-1} after 18 h, hinting at the presence of a hidden LS* state. Upon warming, the $\chi_M T$ value gradually increases to 0.61 cm^3 K mol^{-1} at 32 K, slightly decreases to 0.58 cm^3 K mol^{-1} at 52 K and then quickly returns to the thermal equilibrium state at 74 K. The maximum of $\partial(\chi_M T)/\partial T$ suggests a reverse-LIESST temperature of 66 K. Therefore, **1** exhibits a rare bidirectional LIESST effect, which provides an opportunity to regulate the tristability.

Fluorescence properties

To verify the correlation between luminescence and SCO behavior, temperature-dependent fluorescence emission spectra for **1** and **2** were measured in the heating mode with a 2 K temperature interval in the range of 70–150 K and a 5 K interval in the range of 150–300 K (Fig. 3). An excitation wavelength of 338 nm determined from the excitation spectrum of **1** at 300 K was used for the investigation of fluorescence emission spectra of **1**, **2**, the pyrene guest and the dpoda ligand (Fig. 3 and S23–S26†).

At 300 K, a sharp peak at 392 nm and two broad peaks at 470 and 530 nm are observed for **1** upon excitation at 338 nm (Fig. S23†). However, the peak at 392 nm is very weak in **2** at 300 K. Instead, a more pronounced broad peak appears at 484 nm in **2** (Fig. 3). It is well known that pyrene monomer fluorescence bands can be observed below 400 nm in a very dilute solution.[49] In contrast, the broad and red-shifted excimer fluorescence bands are observed at high concentration, which are formed by the association of excited and unexcited pyrene molecules (Fig. S26†).[50] Moreover, pyrene can interact with solutes or other aromatic molecules to form broad and red-shifted exciplex

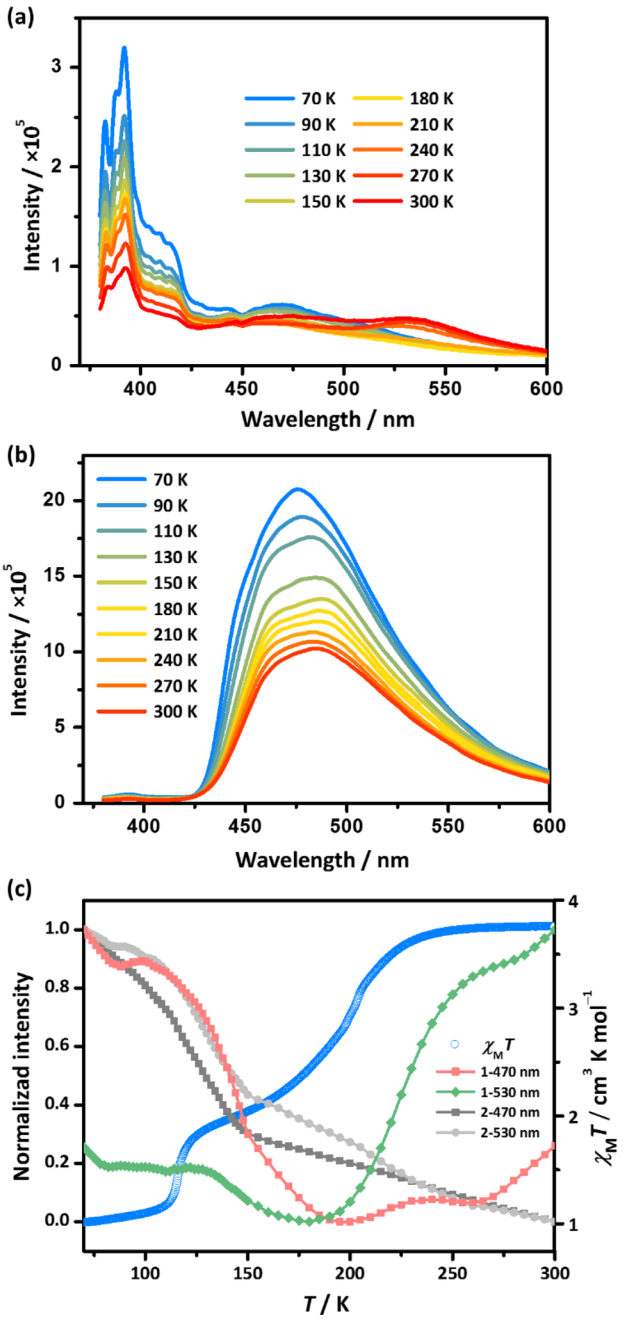

Fig. 3 Variable-temperature fluorescence emission spectra for **1** (a) and **2** (b) from 70 to 300 K; temperature-dependent fluorescence intensities at 470 and 530 nm for **1** and **2** and magnetic data for **1** (c).

fluorescence bands.[51,52] Meanwhile, a sharp peak at 382 nm and a broad band at 434 nm are observed for the dpoda ligand in ethanol at 2.5 μM and 25 mM, respectively. Hence, the pyrene monomer and dpoda monomer contribute to the emission intensity of the sharp peak at 392 nm in **1**.

Reminiscent of the requirement to generate excimer emission in the solid state, the aromatic molecules must be ordered pairwise in parallel planes.[53] The strong intermolecular π···π interaction between them is a key prerequisite for excimer fluorescence.[54] Therefore, it can be inferred that the T-shaped

Open Access Article. Published on 14 May 2024. Downloaded on 1/12/2026 4:43:35 AM. This article is licensed under a Creative Commons Attribution-NonCommercial 3.0 Unported Licence.

arrangement of aromatic molecules with weak C–H···π interactions can be precluded to form the excimer. The crystal data of **1** and **2** at 260 K show that the dpoda ligands are well separated in the 3D framework. Only one type of C–H···π interaction is found between pyridine and 1,3,4-oxadiazole units from two interpenetrating 3D frameworks, illustrating a weak host–host interaction (Fig. S12 and S13†). Hence, the possibility of the dpoda excimer can be ruled out in **1** and **2**.

Meanwhile, the pyrene guests are well separated by the dpoda ligands. Only the T-shaped arrangement of the ordered and disordered pyrene guests with one type of weak C–H···π interaction is found in the crystal (Fig. S12 and S13†), which precludes the presence of a pyrene excimer. Therefore, the broad and red-shifted fluorescence bands at 470 and 530 nm in **1** and at 484 nm in **2** should result from the exciplex emission between pyrene guests and dpoda hosts *via* offset face-to-face π···π interactions (Fig. S12 and S13†). Moreover, the intensities of exciplex bands in **1** are significantly weaker than that in **2**, which should be due to the increased overlap between the absorption and exciplex emission properties in **1** (Fig. S27†).

The temperature-dependent fluorescence spectra show that the monomer and exciplex bands of **1** exhibit different trends as a function of temperature, which are also different from the respective trends of the isostructural compound **2** and pure pyrene in the solid state (Fig. 3 and S28). The emission intensities of **1** at 392 nm basically decrease upon heating, which is due to the effect of thermal quenching. Unlike monomer fluorescence, exciplex fluorescence of **1** at 470 and 530 nm exhibit complicated changes. The emission intensities at 470 nm basically decrease from 70 to 200 K due to thermal quenching along with an unusual plateau between 98 and 88 K, and then gradually increase from 200 to 300 K along with an abnormal plateau between 260 and 240 K. Meanwhile, the emission intensities at 530 nm gradually decrease from 70 to 180 K along with a plateau between 128 and 82 K, and then rapidly increase between 180 and 300 K along with a slope change at 280 K.

In contrast to the complicated and stepped exciplex fluorescence in **1**, the intensities at 470 and 530 nm in the non-SCO derivative **2** almost linearly decrease from 70 to 150 K and then from 150 to 300 K with different slopes, which are mainly due to thermal quenching. Reminiscent of the intense and low-intense d–d transition bands in the Vis and NIR regions for the respective LS and HS states,[30,31] the exciplex fluorescence overlaps more with the LS absorption bands than the HS ones. The transition from LS to HS states results in an increase in emission intensities upon heating, which is contrary to the effect of thermal quenching. Hence, the competition of the influences of the SCO process and thermal quenching results in a general trend of decreasing and then increasing exciplex fluorescence intensities upon heating in **1**. An almost linear decrease of fluorescence intensities at 470 and 530 nm due to thermal quenching is observed in **2**. However, the spin transition process is non-linear and stepped. Moreover, different offset face-to-face π···π interactions between pyrene guests and dpoda hosts result in different red-shifted bands. The SCO process and thermal quenching should have different increasing and decreasing rates of fluorescence intensities for these exciplex bands, resulting in stepped exciplex fluorescence at 470 and 530 nm with different trends and plateau positions in **1**.[38,39] Hence, the complicated and stepped exciplex fluorescence is correlated with two-step SCO behavior.

Dielectric properties

Thermal variations of the dielectric constant were measured from 90 to 290 K at 10 kHz, 100 kHz and 1 MHz frequencies to reveal the unusual dielectric properties (Fig. 4 and S31). The value of the real part (ε') at 1 MHz is almost constant between 90 and 103 K and then gradually decreases between 103 and 122 K. This phenomenon of the decrease of ε' with increasing temperatures is similar to that in the quantum paraelectrics $SrTiO_3$ and $KTaO_3$.[55,56] Upon further warming, the ε' increases almost linearly until 225 K and then suddenly drops to the lowest value at 228 K. Then, it exhibits a frequency dependent increase at higher temperature. Since the HS molecules with four unpaired electrons are more voluminous and distorted than the LS ones, an increase in ε' with increasing temperatures is usually observed for SCO compounds during the LS to HS transition. Hence, the stepped dielectric properties below 228 K in **1** are unusual, which is rare in the SCO field.[57–60]

In order to explore the nature of dielectric properties, crystal data of **1** at 203 and 198 K are first analysed in detail (Table S1†). The space group changes from the centrosymmetric *Pbca* at 203 K to the chiral $P2_12_12_1$ at 198 K, indicating the presence of a phase transition. Meanwhile, the disordered pyrene at 203 K becomes two ordered unique pyrene guests at 198 K. In contrast, the diamagnetic derivative **2** remains in the same centrosymmetric *Pbca* at 203 and 198 K, which still contains the disordered pyrene. In **1**, two unique Fe(II) ions at 203 K become four unique Fe(II) ions at 198 K. The average Fe–N bond distances are 2.100/2.166 Å and 2.015/2.155/2.160/2.151 Å at 203 and 198 K, respectively, illustrating a spin transition process. Hence, we can infer that the symmetric breaking in **1** is induced by the SCO behavior. This phase transition is further confirmed by the differential scanning calorimetry (DSC) measurement at 10 K min^{-1}. It shows an exothermic/endothermic peak at 203/206 K in the cooling/heating mode, which is close to the spin

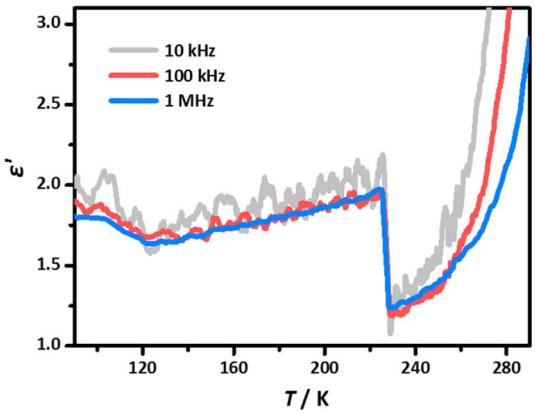

Fig. 4 Variation of the dielectric constant of **1** at 10 kHz, 100 kHz and 1 MHz in the heating mode.

 © 2024 The Author(s). Published by the Royal Society of Chemistry

Open Access Article. Published on 14 May 2024. Downloaded on 1/12/2026 4:43:35 AM. This article is licensed under a Creative Commons Attribution-NonCommercial 3.0 Unported Licence.

transition temperature of 204 K obtained from magnetic susceptibility measurement. The slight temperature differences between SC-XRD, DSC and magnetic measurements may be due to the different scanning rates. However, the structural phase transition temperature is far from the temperature range of 225–228 K where dielectric properties change abruptly, which is out of the range of the temperature lag inherent in the device/sample system. The abrupt drop of ε' between 225 and 228 K in **1** is contrary to the usual increase in ε' upon heating in most SCO compounds,[59] which is also different from the anomaly of ε' observed in molecular ferroelectrics due to the ferroelectric-to-paraelectric phase transition.[61]

The structural parameters of **1** can provide clues to illustrate the nature of the unusual dielectric properties. The octahedral distortion parameters Σ at 260 K are 18.2 and 14.0° for two unique HS Fe1 and Fe2, respectively. However, they change to 21.4 and 17.7° for Fe1 and Fe2 with the average Fe–N bond distances of 2.10 and 2.17 Å at 203 K, which are in the mixed spin and HS states, respectively. This means that the transition from HS to LS for partial Fe(II) ions results in a more distorted coordination environment in this stepped SCO compound. Hence, according to the Σ values, the ε' value at 203 K should be higher than that at 260 K, which competes with the effect of thermal contraction and results in an increase in ε' upon cooling. However, the SCO behavior is gradual upon cooling from 260 to 203 K, which can't explain the abrupt increase in the ε' value between 225 and 228 K. The ε' value should be related to all the components of the structure. Since the space group is the same at 260 and 203 K, the structural phase transition in this temperature range can be excluded. Upon cooling, the LS component is increased. However, the mixed spin state of the Fe1 ion at 203 K hints that only the averaged Fe–N bond distance can be observed in the *Pbca* space group, which prevents to know the exact structure only with the pure LS and HS Fe(II) ions. Hence, the ε' value at 203 K is higher than that at 260 K, which can be inferred from the Σ value. However, the nature of the abrupt increase in the ε' value between 225 and 228 K is still unknown.

When the temperature decreases from 203 to 198 K, a phase transition from *Pbca* to $P2_12_12_1$ is observed. At 198 K, the average Fe–N bond distances are 2.02, 2.16, 2.16 and 2.15 Å for four unique Fe1–Fe4 ions, respectively, which are close to those for one LS and three HS Fe(II) ions. The Σ values are 20.3, 22.0, 21.1 and 22.9° for Fe1–Fe4 ions, respectively, which show the more distorted coordination environments around the Fe(II) ions at 198 K than those at 203 K. However, the disordered pyrene guest at 203 K becomes ordered at 198 K, which contributes to the decrease in ε'. The dielectric properties are related to the contributions of all components in the crystal. Hence, the influences of the disorder-order transition of the pyrene guest and thermal contraction compete with that of Σ and result in a slight decrease in ε' when cooling from 203 to 198 K.

The stepped dielectric properties in the lower temperature region seem to be related to the step SCO behavior from the magnetic data. The $\chi_M T$ value rapidly decreases from 125 to 105 K with a spin transition temperature of 117 K. Meanwhile, the ε' increases from 122 to 103 K, which is consistent with the stepped SCO behavior. The Σ values at 145 K are 21.7, 9.5, 17.2 and 20.5° for Fe1–Fe4 ions, respectively, corresponding to the $HS_{0.5}LS_{0.5}$ state. Meanwhile, the Σ values at 100 K change to 18.7, 10.2, 17.1 and 21.3°, respectively, corresponding to the $HS_{0.25}LS_{0.75}$ state. The distributions of Σ in the $HS_{0.5}LS_{0.5}$ and $HS_{0.25}LS_{0.75}$ states are more fluctuant than that in the HS state, resulting in a higher ε' at lower temperature. Hence, the unusual dielectric properties with higher ε' at lower temperature may be correlated with the more frustrated Σ values in the intermediate spin states.

Conclusions

In summary, we integrate the bent bridging ligand and fluorescent pyrene guest into a 3D Hofmann-type MOF to develop the multifunctional SCO material. The magnetic data show an incomplete and two-step SCO behavior with the sequence of $\gamma_{HS} = 1 \leftrightarrow 1/2 \leftrightarrow 1/4$. However, the crystal data at 198 K illustrate the presence of a hidden $HS_{0.75}LS_{0.25}$ state. The 3D MOF with an incomplete and step SCO behavior provides a good platform to observe the unique bi-directional LIESST *via* 532 and 830 nm light irradiation. The rare stepped thermal relaxation after LIESST is also observed, which has the intermediate 1HS : 1LS state. In comparison with the monomer fluorescence at 392 nm, the complicated and stepped exciplex fluorescence at 470 and 530 nm originated from the offset face-to-face π···π interactions between the pyrene guest and dpoda host is related to the stepped SCO properties. Moreover, the unusual dielectric properties with higher ε' at lower temperature may be correlated with the more frustrated Σ values in the intermediate spin states. Hence, bi-directional LIESST, light-induced stepped thermal relaxation, exciplex fluorescence and dielectric anomalies are integrated into a stepped SCO compound for the first time. The combination of Hofmann-type MOFs with bent pillar ligands and fluorescent guests will provide an excellent platform for the development of multifunctional SCO materials with promising applications in optomagnetic and electromagnetic devices.

Experimental section

Synthesis of [Fe(dpoda){Au(CN)$_2$}$_2$]·pyrene (1)

All the reagents were commercially available and used without further purification. The dpoda ligand (0.0075 g, 0.02 mmol) and K[Au(CN)$_2$] (0.0115 g, 0.04 mmol) in 1 mL of *N*,*N*-diethylformamide (DEF) and $Fe(ClO_4)_2 \cdot 6H_2O$ (0.0180 g, 0.02 mmol) in 1 mL of ethanol were separately added to two arms of a H tube. A saturated solution of pyrene in ethanol was then slowly added to the H-tube. Yellow crystals were obtained after one month. Anal. calcd for $C_{32}H_{18}Au_2FeN_8O$: C, 39.21; H, 1.85; N, 11.43. Found: C, 39.20; H, 2.16; N, 11.33. IR (KBr pellet, cm^{-1}): 3039 (w), 2923 (w), 2355 (w), 2170 (s), 1935 (w), 1616 (m), 1483 (m), 1425 (s), 1009 (m), 1837 (s), 711 (s), 478 (m).

Synthesis of [Zn(dpoda){Au(CN)$_2$}$_2$]·pyrene (2)

The dpoda ligand (0.0074 g, 0.02 mmol) and K[Au(CN)$_2$] (0.0115 g, 0.04 mmol) in 1 mL of *N*,*N*-diethylformamide (DEF)

Open Access Article. Published on 14 May 2024. Downloaded on 1/12/2026 4:43:35 AM. This article is licensed under a Creative Commons Attribution-NonCommercial 3.0 Unported Licence.

and $Zn(ClO_4)_2 \cdot 6H_2O$ (0.0180 g, 0.02 mmol) in 1 ml of ethanol were added to a 5 ml tube and 30 ml vial, respectively. The small tube was placed in the large vial and diffused with a saturated solution of pyrene in ethanol. White crystals were obtained after approximately 10 days. IR (KBr pellet, cm^{-1}): 3040 (w), 2177 (s), 1617 (m), 1485 (m), 1426 (m), 1087 (s), 838 (s), 712 (s), 627 (s).

Physical characterization

The FT-IR spectra were collected in the range of 4000–400 cm^{-1} on a Thermo Nicolet AVTAR 330 FT-IR spectrometer with KBr pellets. C, H and N microanalyses were performed on an Elementar Vario-EL CHNS elemental analyzer. Thermogravimetric (TG) analyses were recorded under a nitrogen flow at a heating rate of 10 K min^{-1} from ambient temperature to 800 °C on a PerkinElmer TGA7 thermogravimetric analyzer. The powder XRD patterns were collected by using a Rigaku SmartLab X-ray diffractometer with CuKα (λ = 1.54178 Å) radiation. UV-vis absorption spectra for the solid sample of **1** ($BaSO_4$ as background) and the liquid sample of the dpoda ligand were recorded in the range of 200–800 nm on a Shimadzu UV-3600 Plus UV-VIS-NIR spectrophotometer equipped with an integrating sphere. The fluorescence spectra for the solid or liquid samples were measured on an Edinburgh FL 980 fluorescence spectrophotometer equipped with a xenon lamp and connected to an ARS cryostat. The Savitzky–Golay method with a window point of 10 was used in OriginPro 8.5 software to smooth the fluorescence curve without changing the actual fluorescence properties. Differential scanning calorimetry (DSC) was performed by cooling and heating the crystals in aluminum crucibles on a NETZSCH-204 at a sweep rate of 10 K min^{-1} under a nitrogen flow. The complex dielectric permittivity was measured on a TH2828A impedance analyzer over the frequency range of 10 kHz to 1 MHz with an applied electric field of 0.5 V. Without changing the actual dielectric properties, the Savitzky–Golay method with a window point of 10 was used to smooth the dielectric curves in OriginPro 8.5 software.

X-ray crystallography

Variable temperature single crystal X-ray diffraction data of **1** were collected on a Bruker D8 QUEST diffractometer with Mo-K_α (λ = 0.71073 Å) radiation at 100, 145 and 260 K, respectively. The data indexing and integration processes were performed using the Bruker APEX-IV software. The structures were solved using the SHELXT structure solution program.[62] All non-hydrogen atoms with anisotropic displacement parameters were refined in the SHELXL refinement package using least squares minimization in OLEX2.[63,64] The hydrogen atoms were refined using a riding model. The crystallographic data are deposited in the Cambridge Crystallographic Data Centre (CCDC). The deposition numbers are 2322894–2322896, 2340544, 2345335, 2345336 and 2352145–2352148.

Magnetic measurements

Magnetic susceptibility data for the dry samples of **1** were collected at 2 K min^{-1} using a Quantum Design MPMS3 SQUID magnetometer under an applied field of 5000 Oe. Pascal's coefficients were used to calculate the diamagnetic correction. For the photomagnetic experiments, a standard fiber optic sample holder (FOSH) was filled with the crystalline sample (~1 mg) and irradiated at 532 and 830 nm (~20 mW cm^{-2}). The exact sample mass was corrected by using magnetic susceptibility data based on a larger amount of the sample (22.2 mg).

Data availability

All data are available in the ESI† and from the authors upon request.

Author contributions

Y.-L. Chen synthesized the compounds and prepared the manuscript. T.-T. Ying performed the dielectric permittivity measurements. Y.-C. Chen performed the magnetic measurements. P.-Y. Liao performed the fluorescence measurements. Z.-P. Ni and M.-L. Tong directed this project and revised the manuscript.

Conflicts of interest

There are no conflicts to declare.

Acknowledgements

This work was supported by the NSFC (22075323 and 21821003).

References

1 P. Gütlich, Y. Garcia and H. A. Goodwin, *Chem. Soc. Rev.*, 2000, **29**, 419–427.
2 P. Gütlich and H. A. Goodwin, *Topics in Current Chemistry*, Springer-Verlag, Berlin Heidelberg, NewYork, 2004, vol. 233–235.
3 A. Bousseksou, G. Molnár, L. Salmon and W. Nicolazzi, *Chem. Soc. Rev.*, 2011, **40**, 3313–3335.
4 M. C. Muñoz and J. A. Real, *Coord. Chem. Rev.*, 2011, **255**, 2068–2093.
5 M. A. Halcrow, *Spin-Crossover Materials: Properties and Applications*, John Wiley & Sons, 2013.
6 Z.-P. Ni, J.-L. Liu, M. N. Hoque, W. Liu, J.-Y. Li, Y.-C. Chen and M.-L. Tong, *Coord. Chem. Rev.*, 2017, **335**, 28–43.
7 M. Feng, Z.-Y. Ruan, Y.-C. Chen and M.-L. Tong, *Chem. Commun.*, 2020, **56**, 13702–13718.
8 M. Piedrahita-Bello, X. Yang, S. E. Alavi, G. Molnár, L. Salmon and A. Bousseksou, *Sens. Actuators, B*, 2023, **393**, 134147.
9 E. Resines-Urien, E. Fernandez-Bartolome, A. Martinez-Martinez, A. Gamonal, L. Piñeiro-López and J. S. Costa, *Chem. Soc. Rev.*, 2023, **52**, 705–727.
10 M. Shatruk, H. Phan, B. A. Chrisostomo and A. Suleimenova, *Coord. Chem. Rev.*, 2015, **289**, 62–73.
11 N. Ortega-Villar, M. C. Muñoz and J. A. Real, *Magnetochemistry*, 2016, **2**, 16.

 © 2024 The Author(s). Published by the Royal Society of Chemistry

Open Access Article. Published on 14 May 2024. Downloaded on 1/12/2026 4:43:35 AM.
This article is licensed under a Creative Commons Attribution-NonCommercial 3.0 Unported Licence.

12 J. E. Clements, J. R. Price, S. M. Neville and C. J. Kepert, *Angew. Chem., Int. Ed.*, 2016, **55**, 15105–15109.
13 N. F. Sciortino, K. A. Zenere, M. E. Corrigan, G. J. Halder, G. Chastanet, J. F. Letard, C. J. Kepert and S. M. Neville, *Chem. Sci.*, 2017, **8**, 701–707.
14 W. Liu, Y.-Y. Peng, S.-G. Wu, Y.-C. Chen, M. N. Hoque, Z.-P. Ni, X.-M. Chen and M.-L. Tong, *Angew. Chem., Int. Ed.*, 2017, **56**, 14982–14986.
15 C.-J. Zhang, K.-T. Lian, G.-Z. Huang, S. Bala, Z.-P. Ni and M.-L. Tong, *Chem. Commun.*, 2019, **55**, 11033–11036.
16 Y.-Y. Peng, S.-G. Wu, Y.-C. Chen, W. Liu, G.-Z. Huang, Z.-P. Ni and M.-L. Tong, *Inorg. Chem. Front.*, 2020, **7**, 1685–1690.
17 S. Decurtins, P. Gütlich, C. P. Köhler, H. Spiering and A. Hauser, *Chem. Phys. Lett.*, 1984, **105**, 1–4.
18 A. Hauser, *Chem. Phys. Lett.*, 1986, **124**, 543–548.
19 A. Hauser, J. Jeftić, H. Romstedt, R. Hinek and H. Spiering, *Coord. Chem. Rev.*, 1999, **190–192**, 471–491.
20 A. Hauser, in *Spin Crossover in Transition Metal Compounds II*, Springer Berlin Heidelberg, Berlin, Heidelberg, 2004, pp. 155–198, DOI: 10.1007/b95416.
21 E. Milin, V. Patinec, S. Triki, E.-E. Bendeif, S. Pillet, M. Marchivie, G. Chastanet and K. Boukheddaden, *Inorg. Chem.*, 2016, **55**, 11652–11661.
22 T. Boonprab, S. J. Lee, S. G. Telfer, K. S. Murray, W. Phonsri, G. Chastanet, E. Collet, E. Trzop, G. N. L. Jameson, P. Harding and D. J. Harding, *Angew. Chem., Int. Ed.*, 2019, **58**, 11811–11815.
23 M. Ahmed, K. A. Zenere, N. F. Sciortino, K. S. A. Arachchige, G. F. Turner, J. Cruddas, C. Hua, J. R. Price, J. K. Clegg, F. J. Valverde-Muñoz, J. A. Real, G. Chastanet, S. A. Moggach, C. J. Kepert, B. J. Powell and S. M. Neville, *Inorg. Chem.*, 2022, **61**, 6641–6649.
24 K.-P. Xie, Z.-Y. Ruan, X.-X. Chen, J. Yang, S.-G. Wu, Z.-P. Ni and M.-L. Tong, *Inorg. Chem. Front.*, 2022, **9**, 1770–1776.
25 K. D. Murnaghan, C. Carbonera, L. Toupet, M. Griffin, M. M. Dîrtu, C. Desplanches, Y. Garcia, E. Collet, J. F. Létard and G. G. Morgan, *Chem.–Eur. J.*, 2014, **20**, 5613–5618.
26 K.-P. Xie, Z.-Y. Ruan, B.-H. Lyu, X.-X. Chen, X.-W. Zhang, G.-Z. Huang, Y.-C. Chen, Z.-P. Ni and M.-L. Tong, *Angew. Chem., Int. Ed.*, 2021, **60**, 27144–27150.
27 V. Jornet-Mollá, C. Giménez-Saiz, L. Cañadillas-Delgado, D. S. Yufit, J. A. K. Howard and F. M. Romero, *Chem. Sci.*, 2021, **12**, 1038–1053.
28 M. Seredyuk, K. Znovjyak, F. J. Valverde-Muñoz, M. C. Muñoz, V. M. Amirkhanov, I. O. Fritsky and J. A. Real, *Inorg. Chem.*, 2023, **62**, 9044–9053.
29 Y.-C. Chen, Y. Meng, Y.-J. Dong, X.-W. Song, G.-Z. Huang, C.-L. Zhang, Z.-P. Ni, J. Navařík, O. Malina, R. Zbořil and M.-L. Tong, *Chem. Sci.*, 2020, **11**, 3281–3289.
30 H. J. Shepherd, C. M. Quintero, G. Molnár, L. Salmon and A. Bousseksou, in *Spin-Crossover Materials: Properties and Application*, ed M. A. Halcrow, John Wiley & Sons Ltd, 2013, pp. 347–373.
31 M. K. Javed, A. Sulaiman, M. Yamashita and Z.-Y. Li, *Coord. Chem. Rev.*, 2022, **467**, 214625.
32 Y. Garcia, F. Robert, A. D. Naik, G. Zhou, B. Tinant, K. Robeyns, S. Michotte and L. Piraux, *J. Am. Chem. Soc.*, 2011, **133**, 15850–15853.
33 S. Titos-Padilla, J. M. Herrera, X.-W. Chen, J. J. Delgado and E. Colacio, *Angew. Chem., Int. Ed.*, 2011, **50**, 3290–3293.
34 C.-F. Wang, R.-F. Li, X.-Y. Chen, R.-J. Wei, L.-S. Zheng and J. Tao, *Angew. Chem., Int. Ed.*, 2015, **54**, 1574–1577.
35 J.-L. Wang, Q. Liu, X.-J. Lv, R.-L. Wang, C.-Y. Duan and T. Liu, *Dalton Trans.*, 2016, **45**, 18552–18558.
36 C. Lochenie, K. Schötz, F. Panzer, H. Kurz, B. Maier, F. Puchtler, S. Agarwal, A. Köhler and B. Weber, *J. Am. Chem. Soc.*, 2018, **140**, 700–709.
37 J.-L. Wang, Q. Liu, Y.-S. Meng, X. Liu, H. Zheng, Q. Shi, C.-Y. Duan and T. Liu, *Chem. Sci.*, 2018, **9**, 2892–2897.
38 J. Yuan, S.-Q. Wu, M.-J. Liu, O. Sato and H.-Z. Kou, *J. Am. Chem. Soc.*, 2018, **140**, 9426–9433.
39 J.-Y. Ge, Z. Chen, L. Zhang, X. Liang, J. Su, M. Kurmoo and J.-L. Zuo, *Angew. Chem., Int. Ed.*, 2019, **58**, 8789–8793.
40 B. Benaicha, K. Van Do, A. Yangui, N. Pittala, A. Lusson, M. Sy, G. Bouchez, H. Fourati, C. J. Gómez-García, S. Triki and K. Boukheddaden, *Chem. Sci.*, 2019, **10**, 6791–6798.
41 K. Sun, J.-P. Xue, Z.-S. Yao and J. Tao, *Dalton Trans.*, 2022, **51**, 16044–16054.
42 J. Wang, M. Kong, X.-J. Song, Y. Jing, Y. Zhao and Y. Song, *Inorg. Chem.*, 2022, **61**, 20923–20930.
43 G. Yang, S.-G. Wu, Z.-Y. Ruan, Y.-C. Chen, K.-P. Xie, Z.-P. Ni and M.-L. Tong, *Angew. Chem., Int. Ed.*, 2023, **62**, e202312685.
44 N. Mataga, H. Chosrowjan and S. Taniguchi, *J. Photochem. Photobiol., C*, 2005, **6**, 37–79.
45 Z. Wang, C. Wang, H. Zhang, Z. Liu, B. Zhao and W. Li, *Org. Electron.*, 2019, **66**, 227–241.
46 B.-H. Zhang and Z.-Y. Xie, *Front. Chem.*, 2019, **7**, 306.
47 J. Li, Z. Li, H. Liu, H.-Q. Gong, J.-C. Zhang and Q. Guo, *Front. Chem.*, 2022, **10**, 952116.
48 T. Delgado, M. Meneses-Sánchez, L. Piñeiro-López, C. Bartual-Murgui, M. C. Muñoz and J. A. Real, *Chem. Sci.*, 2018, **9**, 8446–8452.
49 K. Kalyanasundaram and J. K. Thomas, *J. Am. Chem. Soc.*, 1977, **99**, 2039–2044.
50 J. B. Birks and L. G. Christophorou, *Nature*, 1962, **194**, 442–444.
51 M. Meneses-Sánchez, L. Piñeiro-López, T. Delgado, C. Bartual-Murgui, M. C. Muñoz, P. Chakraborty and J. A. Real, *J. Mater. Chem. C*, 2020, **8**, 1623–1633.
52 B. D. Wagner, G. J. McManus, B. Moulton and M. J. Zaworotko, *Chem. Commun.*, 2002, 2176–2177.
53 M. Schwoere and H. C. Wolf, *Organic Molecular Solids*, WILEY-VCH Verlag GmbH & Co. KGaA, Weinheim, 2007.
54 Y. Ge, Y. Wen, H. Liu, T. Lu, Y. Yu, X. Zhang, B. Li, S.-T. Zhang, W. Li and B. Yang, *J. Mater. Chem. C*, 2020, **8**, 11830–11838.
55 G. A. Samara, *J. Phys.: Condens. Matter*, 2003, **15**, R367–R411.
56 M. Itoh and H. Taniguchi, in *Structure and Bonding*, Springer Berlin, Heidelberg, 2007, vol. 46, pp. 89–118.
57 A. Bousseksou, G. Molnár, P. Demont and J. Menegotto, *J. Mater. Chem.*, 2003, **13**, 2069–2071.

Open Access Article. Published on 14 May 2024. Downloaded on 1/12/2026 4:43:35 AM.
This article is licensed under a Creative Commons Attribution-NonCommercial 3.0 Unported Licence.

58 S. Bonhommeau, T. Guillon, L. M. Lawson Daku, P. Demont, J. Sanchez Costa, J. F. Létard, G. Molnár and A. Bousseksou, *Angew. Chem., Int. Ed.*, 2006, **45**, 1625–1629.
59 C. Lefter, V. Davesne, L. Salmon, G. Molnár, P. Demont, A. Rotaru and A. Bousseksou, *Magnetochemistry*, 2016, **2**, 18.
60 Y.-R. Qiu, L. Cui, P.-Y. Cai, F. Yu, M. Kurmoo, C. F. Leong, D. M. D'Alessandro and J.-L. Zuo, *Chem. Sci.*, 2020, **11**, 6229–6235.
61 P.-P. Shi, Y.-Y. Tang, P.-F. Li, W.-Q. Liao, Z.-X. Wang, Q. Ye and R.-G. Xiong, *Chem. Soc. Rev.*, 2016, **45**, 3811–3827.
62 G. M. Sheldrick, *Acta Crystallogr., Sect. A: Found. Adv.*, 2015, **71**, 3–8.
63 G. M. Sheldrick, *Acta Crystallogr., Sect. A: Found. Crystallogr.*, 2008, **64**, 112–122.
64 O. V. Dolomanov, L. J. Bourhis, R. J. Gildea, J. A. K. Howard and H. Puschmann, OLEX2: a complete structure solution, refinement and analysis program, *J. Appl. Crystallogr.*, 2009, **42**, 339–341.

 © 2024 The Author(s). Published by the Royal Society of Chemistry